https://doi.org/10.1016/j.compositesa.2022.107211

On the Properties and Deterioration Mechanism of Fibre-Matrix Interfaces of FRP Composites Under Coupled Thermal-Mechanical Actions

Kui Lin and Tao Yu*

Department of Civil and Environmental Engineering,
The Hong Kong Polytechnic University, Hong Kong, China. Email: tao-cee.yu@polyu.edu.hk

Abstract:

The kinetic theory is often used to evaluate the long-term performance of fibre-reinforced polymer (FRP) composites. However, the fundamental deterioration mechanism of the fibre-matrix interfaces, which may change significantly with temperature, has not been rigorously examined. This paper presents a study to address this deficiency of existing studies using reactive force field molecular dynamics simulations. Two models were established for the untreated and sizing-treated fibre-matrix interfaces, respectively, and performed debonding simulations over a wide range of temperatures. The simulations were validated with the previous experimental results in various terms and were used to quantitatively examine the effects of coupled thermal-mechanical actions on the key properties of the interfaces and their deterioration mechanism which involves the breakage of covalent bonds. The results shed light on the design and interpretation of accelerated tests and may be used in multiscale and multifield modelling of the durability of FRP composites in the future.

Keywords: FRP; sizing; interfacial debonding; thermal-mechanical coupling

1. INTRODUCTION

Fibre-reinforced polymer (FRP) composites have been widely used in the aerospace, automotive, and marine industries [1] and are gaining increasing acceptance in civil infrastructure construction [2]. Thermosetting resins are extensively used as the polymeric matrix of FRP composites due to their excellent properties including the relatively high stiffness and solvent resistance [3]. Compared with thermoplastic resins, thermosets generally have a higher softening temperature and superior creep resistance [4]. However, thermosets are still characterized by the glass transition and entropic elasticity of polymers, which makes temperature a crucial factor affecting their properties [5, 6].

In the durability studies of FRP composites, accelerated laboratory exposure tests have been widely adopted, in which the specimens are commonly subjected to an elevated temperature to accelerate their deterioration [7-11]. The results from the accelerated exposure tests are often used to predict the long-term performance of FRP composites by adopting the Arrhenius equation [12], which describes the relationship between the deterioration rates of a material subjected to different temperatures. The use of the Arrhenius equation assumes that the fundamental deterioration mechanism (e.g., represented by the activation energy [7-10]) does not change in the accelerated exposure tests, but this assumption has not been verified for FRP composites. Due to the characteristics of glass transition and entropic elasticity of the polymeric matrix, it is likely that

the Arrhenius equation may only be valid for a certain temperature range for FRP composites. This temperature range, however, has not yet been clarified or rigorously examined.

The durability of FRP composites depends significantly on the deterioration of the fibre-matrix interfaces which play an important role in the force transfer among the fibres and the matrix [13-17]. Existing experimental studies have shown that the deterioration of fibre-matrix interfaces (e.g., criss-crossing voids [15], adhesive rupture [13], delamination [16]) due to thermal cycles have significant effects on the mechanical properties of FRP composites. Therefore, the thermal-mechanical properties of fibre-matrix interfaces are crucial for durability studies. However, although extensive experimental studies (e.g., Refs.[15, 18-22]) were conducted on the temperature dependence of the properties of polymers, the relevant existing studies on the fibre-matrix interfaces have been limited. The macroscopic experimental studies of the fibre-matrix interfaces (e.g., Refs.[23, 24]) generally failed to separate the intrinsic interfacial properties from the overall test results which were largely controlled by the behaviour of the polymeric matrix. The micro-/nano- in situ experiments (e.g., Refs.[25, 26]) adopting sufficiently thin fibre-matrix interface samples may allow the intrinsic interfacial properties to be explored, but they have been rather limited due to the difficulties in performing the tests (e.g., temperature control and combined thermal-mechanical actions, especially for the high temperature required when the matrix enters the rubbery state). It remains unclear whether the theories derived for the temperature-dependent properties of polymers (e.g., Eyring's theory) are applicable to fibre-matrix interfaces, noting that the interfacial behaviour may be further complicated by the presence of fibre sizing which leads to enhanced covalent bonds at the interfaces.

On the other hand, multiscale modelling using the bottom-up approach has emerged as an effective way to understand and predict the durability of materials [27, 28]. For FRP composites, continuum mechanics-based numerical modelling (e.g., finite element modelling) may be used to simulate their behaviour under combined mechanical and environmental (e.g., thermal) actions if the time- and temperature-dependent properties of fibres, polymeric matrix and fibre-matrix interfaces can be properly defined. The microscopic understanding and properties necessary for numerical modelling at the macroscopic level are difficult to obtain experimentally (e.g., the intrinsic properties of the interface as well as the effects of thermal-mechanical coupling). Molecular dynamics (MD) simulations have been shown to be an effective method to understand microscopic mechanisms and to obtain microscopic properties, which may be used as an alternative method to obtain the interfacial properties under thermal-mechanical coupling conditions [29, 30].

The existing MD studies on fibre-matrix interfaces (e.g., Refs.[31-33]) have mostly been limited to qualitative explanations of the deterioration mechanism of the interfaces in different environments (e.g., moisture and salt); their models are generally not large enough to obtain representative mechanical parameters. Furthermore, in commercial FRP products in civil engineering, it is a common practice to apply a sizing layer (e.g., with a silane coupling agent) on the fibre surfaces. The sizing layer reacts with both the fibre and the matrix (i.e., forming chemical bonds), and thus improves the adhesion between them. It has been shown by the existing studies (e.g., Ref.[34]) that the sizing layer leads to improved durability and mechanical properties. However, the vast majority of MD studies have only considered nonbonding interactions and thus cannot simulate the formation/breakage of covalent bonds under thermal-mechanical actions. To simulate the fibre-matrix interfaces under thermal-mechanical actions, it is also important to clarify

the evolution of the mechanical properties of the interfaces over a wide temperature range and its corresponding microscopic mechanisms so as to provide a comprehensive understanding of these properties when the matrix moves from the glassy to the rubbery state. Therefore, it is essential to use MD simulations with a reactive force field (e.g., ReaxFF) to clarify and quantify the interfacial thermal-mechanical properties for multifield and multiscale coupling modelling, as well as durability studies of FRP composites.

Against this background, this paper presents the first-ever study on the properties and deterioration mechanism of fibre-matrix interfaces under various temperatures in combination with tensile loading using MD simulations; the ReaxFF force field was adopted to capture the roles of covalent bonds, and the interfaces with and without fibre sizing were both simulated to examine their differences. The study covers a wide range of temperatures (300 K∼600 K) which allows the polymeric matrix to be investigated in both the glassy state and the rubbery state; it also allows the glass transition temperature to be determined by the MD simulation results. Importantly, the molecular models are sufficiently large so that the macroscopic interfacial properties (e.g., the peak stress, modulus, and toughness) under various temperatures can be quantitively obtained as the statistical average of microscopic quantities; the validity of this approach has been demonstrated in a previous study by the authors' group [35] on the mechanical properties of fibre-matrix interfaces under typical room temperature (i.e., 300 K). In the following sections, the details of the methods are first presented, followed by interpretations and discussions of the simulation results with reference to the existing theories on polymers (i.e., Eyring's theory and the kinetic theory).

2. METHODS

In this study, the Large-scale Atomic/Molecular Massively Parallel Simulator (LAMMPS) [36] was adopted to construct the MD models, to perform ReaxFF MD simulations for obtaining the glass transition temperature (T_g) and for the tension process at fibre-matrix interfaces. The consistent valence force field (CVFF) [35] was used only in the model construction process as the only purpose of that process was to construct the cross-linked interface model. After the cross-linked model was constructed, the ReaxFF forcefield [37] was used to carry out structural relaxation and to calculate the glass transition properties. The same force field (i.e., ReaxFF forcefield) was also used in the subsequent debonding process to ensure the reliability of the results. In all the simulations, the van der Waals interactions were calculated with a cutoff distance of 12 Å and the electrostatic interactions were described by the Ewald method with a cutoff distance of 10 Å. These cutoff distances are sufficiently large to describe the nonbonding interactions [38]. Details of the models and the simulation methods are presented below.

2.1. Construction of Models

An untreated fibre (i.e., without sizing)-matrix model and a sizing-treated fibre-matrix model were constructed in this study. For the former, the construction process involved only cross-linking of polymer monomers on the hydroxylated glass fibre surface (Figure 1a); the fibre surface was hydroxylated due to the presence of unsaturated oxygen on the silica surface. By contrast, the construction process of the sizing-treated interface model involved two additional steps: grafting the silane onto the hydroxylated glass fibre surface and then coupling the grafted silane with the

matrix (Figure 1b). It is a common process to produce a sizing-treated fibre [39]. In the two models, the glass fibre was simulated by surface-hydroxylated silica (quartz) with a size of 16.5 × 157.2 × 86.5 Å, while a total of 1600 monomers of diglycidyl ether of bisphenol A (DGEBA) (epoxy) and 1600 monomers of 1,3-Phenylenediamine (mPDA) (curing agent) were adopted to form the polymer matrix by cross-linking. Sixty-four 3-aminopropyltriethoxysilane (APTES) molecules were uniformly grafted onto the fibre surface for the sizing-treated model. The construction process of the models was performed using classical MD simulations with the CVFF force field [35]. The formation of chemical bonds (i.e., cross-linking) between reactive sites (O in the epoxy groups of the DGEBA and N in the amine groups of the mPDA) is assumed to occur when their distance is less than 2.5 Å. The use of this distance ensures that the initial bond forces arising during the process are not overly large while an adequate degree of coupling can be obtained [40]. The cross-linking simulation was performed at 380 K for 0.7 ns as the cross-linking became extremely slow afterwards. After modelling, the density of the matrix was 1.29 g/cm^3 in the untreated fibre-matrix model (degree of cross-linking: 73.9%) and 1.28 g/cm^3 in the sizing-treated fibre-matrix model (degree of cross-linking: 71.4%). These densities are close to the theoretical/experimental results of epoxy resin (DGEBA/mPDA) reported in the previous studies (e.g., Refs [41-43]). The degrees of crosslinking in the two models are within the range of experimental values (e.g., 68% to 79.5% reported by Ref. [44] and 75% to 92% reported by Ref. [45]) and are larger than the conversion at the gel point (67% for the DGEBA/mPDA systems [44]); the gel point represents a critical extent of reaction at which the polymeric matrix transitions from the liquid to the solid state. In addition, the two cross-linking degrees are sufficiently close for the two models to serve in a comparative study. Therefore, the two models can be used for the study of the thermodynamic properties of fibre-matrix interfaces. More details of the models can be found in Ref. [35].

2.2. Determination of Glass Transition Temperature

The glass transition temperature (T_g) of the matrix in the untreated interface model was determined based on the variation of density with temperature, which is a conventional method in MD simulations [46], while the T_g of the matrix in the sizing-treated interface model is expected to be similar due to the similar degree of cross-linking of the matrix in the two models. This method of determining T_g has the same mechanism as the thermo-mechanical analysis (TMA) method which is commonly used in experimental studies; with the TMA, the T_g is determined by the measurement of the dimensional variation of a constant-mass sample with temperature [47].

The variation of density with temperature was obtained by gradually reducing the temperature of the matrix from 600 K to 260 K with a rate of 10 K per 2 ns; this temperature rate was found to be slow enough to reach a stable density at each temperature. In this process, the ReaxFF force field [37] with the NPT (constant number of atoms, pressure and temperature) ensemble was adopted with a timestep of 0.5 fs; periodic boundary conditions in the x, y, and z directions were applied and the pressure was controlled to 1 atm.

2.3. Simulation of Debonding

Following the approach of the authors' previous study [35], a tensioning process was applied to simulate the debonding at the fibre-matrix interfaces. In this process, the top of the matrix was

fixed while a downward velocity of 40 m/s (i.e., by moving 0.01 nm and then relaxing 500 steps) was applied to the bottom of the fibre as shown in Figure 1c. The velocity (or strain rate) is within the range of velocities used in most MD simulations [48, 49], and can reflect the molecular motion mechanism during the debonding process and obtain statistically significant mechanical parameters [48]. It should be noted that except for the rigid bottom two layers of atoms (Figure 1c), the remaining 1.4 nm thickness of the fibre is unfixed. The rigid bottom does not affect the deformation of the fibre surface due to the high modulus of the fibre [50] (i.e., silica); the distance between the rigid part and the matrix is also larger than the cutoff distances, so that the rigid bottom does not affect the nonbonding interactions with the matrix. The middle region (unfixed part) was simulated with the NVE (constant number of atoms, volume and energy) ensemble with a timestep of 0.5 fs while the temperature was controlled at a specific temperature (i.e., 300 K, 320 K, 340 K, 360 K, 380 K, 400 K, 420 K, 440 K, 460 K, 480 K, 520 K, 560 K or 600 K); periodic boundary conditions in the y and z directions were applied. In the simulations, the reactive force field ReaxFF [37] was adopted to obtain the mechanical properties and capture the potential breakage of chemical bonds in the debonding process. The virial stress [51] of the unfixed region of the matrix was recorded every 500 steps, which was then statistically averaged to obtain the so-called true stress or Cauchy stress [51] of the matrix. The so-obtained true stress was then used to plot the stress-displacement curve for which thermal noises were eliminated by a smoothing process [35].

Each model contains approximately 125,000 atoms, and a total of 26 simulation tasks (i.e., 13 temperatures for the models with and without fibre sizing) were performed in this study. The simulations took a total of over 1.2 million computational core hours, making them the largest atomistic computational study of FRP composites in civil engineering at present. The reaction force field and the sufficiently large models ensure that the interactions between atoms are accurate and the models are statistically significant, making the results representative and robust. The simulation results are therefore not only fully representative for understanding the micromechanics of fibre-matrix interfaces but also contribute significantly to multiscale modelling, as discussed in the subsequent section.

3. RESULTS AND DISCUSSIONS

3.1. Glass Transition Temperature

The glass transition temperature (T_g) is the temperature at which increased molecular mobility occurs, leading to significant changes in the thermal properties of amorphous polymers [52]. Polymers are in a glassy state and are capable of forming stable structures at temperatures below the T_g, while they behave as rubbery materials at temperatures above the T_g. In this study, the variation of density of the matrix with temperature was obtained from the MD simulations, as shown in Figure 2 where the dimensionless density values are obtained by dividing the density by the density at 600 K. It is evident that the density decreases with the temperature and there is an apparent change of the rate of decrease at approximately 450 K. Therefore, the T_g of the matrix in this study is determined to be 450 K. This result is close to the experimental result (i.e., $T_g = 446$ K, see [45, 47]) of epoxy resin formed with the same epoxy monomer (DGEBA) and curing agent (mPDA); the experimental result was determined using the TMA approach. The similar T_g values verify the reliability of the force field used in this study in simulating the thermal mobility of the molecules. The molecular morphology of the matrix at various temperatures was then used as the

initial state in the subsequent debonding simulations to ensure consistency in the glass transition properties.

3.2. Debonding of Untreated Fibre-matrix Interface at Various Temperatures

The stress-displacement curves, in which the stress is taken as the true stress (see Section 2.3) while the displacement refers to the downward movement of the fibre measured from its top surface, are shown in Figure 3a for the untreated fibre-matrix interface under the 13 temperatures; Figure 3b-3g show typical snapshots of the interface in the debonding process for different temperatures (i.e., 300 K, 360 K, 420 K, 480 K, 560 K, and 600 K). It is not a surprise to see that the interfacial strength decreases with the temperature (Figure 3a). When the temperature is below or near T_g, the stress decreases sharply after the peak stress, indicating a quasi-brittle fracture mode. By contrast, at a relatively high temperature (>520 K), the stress-displacement curve is featured by a plastic plateau with a length of 1~1.5 nm (See the inset of Figure 3a), suggesting that the rubbery state of the polymer matrix allows for a relatively large degree of plasticity in the debonding process.

The differences in the debonding process of the interface under different temperatures are also evident from the debonding morphologies. As shown in Figure 3b-3g, the debonding process may be described by three motions, which are herein termed cavitation/nucleation (at 0.5~1 nm), plastic yield/flow (at 0.5~2 nm), and bridge rupture/crazing (at 2~4 nm), respectively, following the existing studies [53, 54]. At temperatures well below the T_g, Figures 3b, c show that the interface has already largely deteriorated when cavitation/nucleation occurs (at 1 nm). By contrast, when the temperature is far above T_g (see Figures 3f, g), the matrix and the fibre remain in good contact when the displacement is 1 nm; a large amount of matrix is still adhered to the fibre surface even at an elongation of 2 nm, indicating the large plastic flow capability due to the strong mobility of the matrix in the rubbery state. With the further increase of displacement, rupture of the bridges formed by slipped polymers between the fibre and the matrix occurs, leaving some matrix residuals on the fibre surface. The residual ratio of the matrix on the fibre surface is counted for the 13 temperatures and the results are shown in Figure 3h, where the inserted snapshots illustrate several typical morphologies of the debonded fibre surface. Figure 3h indicates that the residual ratio of the matrix increases with the temperature, especially when the matrix is in a rubbery state. It should be noted that the velocity of separation may affect the fracture morphology, especially for amorphous materials with complex molecular structures. However, this is beyond the scope of the present study which is concerned only with the effects of temperature on the fracture morphology.

To further examine the interfacial debonding characteristics, the morphology of the nonbonding interaction zone is shown in Figure 4a-4d for various temperatures. The nonbonding interaction zone is a region of 1.2 nm from the fibre surface, beyond which the matrix is not subjected to nonbonding interactions (e.g., van der Waals forces and hydrogen bonding) by the fibre and its surface hydroxyl groups. It is evident from Figure 3 that cavitation occurs at the displacement of 0.5 nm, which is approximately the mean displacement at the peak stress for various temperatures. The matrix in the nonbonding zone then rapidly decreases with the displacement, especially for those at temperatures below T_g. With the MD simulation results, the debonding ratio of the nonbonding zone can be calculated by dividing the debonded volume of the matrix by its initial volume in this zone. The so-obtained debonding ratios for interfaces subjected to different

temperatures are compared in Figure 4e for different displacements. It can be seen that when the displacement is 0.5 nm, the debonding ratio remains almost the same in the glassy state while increasing slightly with the temperature in the rubbery state, which may be due to the increasing instability of the interfacial morphology in the rubbery state. However, when the displacement is 1 nm or 2 nm, the debonding ratio decreases with the temperature and the rate of such decrease is significantly higher in the rubbery state due to the increased plastic flow capability.

3.3. Debonding of Sizing-treated Fibre-matrix Interface at Different Temperatures

For the sizing-treated fibre-matrix interface, the covalent bonds between the fibre and the matrix significantly enhance the interfacial connection [35]. Figures 5a-5f show typical snapshots in the debonding process of the interface at different temperatures. It is evident that the sizing can effectively improve the bond at the interface. However, as it is not possible to achieve 100% coverage of the sizing on the fibre surface, the part not covered by the sizing would fail first (see Figure 5a), followed by the cracks in the sizing-connected epoxy. Furthermore, the stress-displacement curves at temperatures from 300 K to 600 K show that there is a plastic plateau of up to 5~6 nm on the curves and the displacement at debonding of the sizing-treated fibre-matrix interface reaches up to 30~50 nm (see Figure 5g), which is an order of magnitude higher than that of the untreated fibre-matrix interface (see Figure 3a).

Similar to the untreated interface, the strength of the sizing-treated fibre-matrix interface decreases with the temperature (Figure 5g). However, as the plastic flow capacity of the latter is already large at a relatively low temperature (i.e., 300 K) (Figure 5g), the effect of temperature on the debonding morphologies of the latter (Figures 5a-5f) appears not as pronounced as that of the former (Figures 3b-3g). A similar observation may be made from Figure 5h which shows the residual ratio of the matrix after bridge rupture for the sizing-treated fibre-matrix interface: the residual ratio still increases with the temperature but to a lesser degree than that in the untreated interface (Figure 3h). It is also worth noting that the residual ratio of the treated interface is generally about 25 to 80 times that of the untreated interface due to the presence of additional covalent bonds in the former.

Figures 6a-6d show the morphological evolutions of the nonbonding interaction zone of the sizing-treated fibre-matrix interface under various temperatures, while the variation of the debonding ratio of this zone with the temperature is shown in Figure 6e for different displacements. By comparing Figures 4 and 6, it is evident that for both interfaces (i.e., with and without fibre sizing), the morphologies, as well as the debonding ratios and their trend with the temperature at the mean displacement corresponding to the peak stress (i.e., 0.6 nm for the sizing-treated fibre-matrix interface), are all similar. This observation suggests that, in the initial stage up to the peak stress, the additional covalent bonds provided by fibre sizing do not play a significant role in the interfacial properties or the debonding process. The role of covalent bonds becomes substantial as the displacement increases: the debonding ratio of the sizing-treated interface ranges from 50% to 80% at 3 nm (see Figure 6e), whereas, for the untreated interface, the debonding ratio is already approximately 90% to 95% at 2 nm (see Figure 4e). Another observation from Figure 6e is that the rate of decrease of the debonding ratio with the temperature does not seem to increase when the temperature exceeds T_g. This is different from the observation in Figure 4e for the untreated interface and is a result of having significant covalent bonds at the interface.

3.4. Quantification of Thermal-mechanical Effects on Fibre-matrix Interfaces

To further understand the interfacial debonding properties, the thermal-mechanical effects on the two fibre-matrix interfaces are quantitatively examined with reference to the existing theories. The stress-nominal strain curves of the two fibre-matrix interfaces are compared in Figure 7a, in which the nominal strain ε was calculated by $\varepsilon = d/L_0$, where L_0 is the initial length of the unfixed matrix at the corresponding temperature and d is the downward displacement of the fibre (i.e., same as plotted in Figures 3a and 5g). As the modulus and strength of the fibre are at least one order of magnitude larger [50] than the corresponding properties of the matrix, the deformation/damage induced by the displacement mainly occurs within the matrix or at the physical interface between the fibre and the matrix.

3.4.1. Peak Stress

Figure 7a shows that before the peak stress is reached, the curves of the two interface models at the same temperature are similar in the glassy state while their difference is evident in the rubbery state. Figure 7b further shows the variations of the peak stress with temperature for the two interfaces. It is evident that in the glassy state, the peak stresses of the untreated and sizing-treated fibre-matrix interfaces are similar and they both decrease almost linearly with temperature. The rates of decrease of the former and the latter in the glassy state are 0.476 MPa/K and 0.475 MPa/K, respectively, based on a linear regression analysis. When the temperature is close to T_g of the matrix, the peak stress somewhat plateaus and does not significantly change until a temperature (i.e., 520 K) is significantly higher than the T_g. After that, the peak stress of both interfaces decreases rapidly with temperature. The rates of decrease in this stage (i.e., rubbery state) are 1.289 MPa/K and 0.723 MPa/K for the untreated and treated interfaces, respectively, which are both significantly higher than the corresponding values in the glassy state. Furthermore, by looking at the two numbers, the untreated interface appears more sensitive to temperature in the rubbery state than the treated interface.

It is worth noting that the linear relationship between the peak stress and the temperature in the two temperature ranges (i.e., < 450 K and > 520 K) is consistent with the implication of the well-known Eyring equation [55] for stress-biased thermal activation. The Eyring equation has been widely and successfully adopted to describe the behaviour of polymers but has not been examined for fibre-matrix interfaces. An approximation of the original Eyring equation for the ranges of temperatures, strain rates, and stresses in the present study can be expressed as [21, 56]:

$$\sigma_{\text{yield}}(T) = \frac{k_{\text{B}}}{v_{\text{a}}} \ln\left(\frac{2\dot{\varepsilon}}{\dot{\varepsilon}_0}\right) T + \frac{E_{\text{a}}}{v_{\text{a}}}, \quad (1)$$

where σ_{yield} is the yield stress and is taken as the peak stress in this study [57], T is the absolute temperature, E_a is the activation energy, v_{a} is the activation volume, $\dot{\varepsilon}$ is the strain rate, $\dot{\varepsilon}_0$ is a rate constant (containing an entropy factor and an elementary shear strain [21]), and k_{B} is the Boltzmann's constant. The second item on the righthand side of Eq. (1) is also referred to as an apparent activation energy density [58], $\rho_{\text{a}} = E_{\text{a}}/v_{\text{a}}$, in the unit of Pa or J/m^3.

Eq. 1 suggests that the term $\frac{k_B}{v_a}\ln\left(\frac{2\dot{\varepsilon}}{\dot{\varepsilon}_0}\right)$ defines the slope of the peak stress-temperature curve (Figure 7b), while the term E_a/v_a (i.e., ρ_a) defines the intercept of the curve with the vertical axis when $T = 0$. By comparing the slopes of the curves given above and in Figure 7b, it can be derived that: (1) the value of $\frac{k_B}{v_a}\ln\left(\frac{2\dot{\varepsilon}}{\dot{\varepsilon}_0}\right)$ is almost a constant when the matrix is in the glassy state and when the temperature is well above the glass transition temperature; (2) the fibre sizing has little effect on the value of $\frac{k_B}{v_a}\ln\left(\frac{2\dot{\varepsilon}}{\dot{\varepsilon}_0}\right)$ in the glassy state; (3) the absolute value of $\frac{k_B}{v_a}\ln\left(\frac{2\dot{\varepsilon}}{\dot{\varepsilon}_0}\right)$ increases when the matrix enters the rubbery state, which is believed to be at least partially due to the difference in the $\dot{\varepsilon}_0$ between the glassy and rubbery states, while the fibre sizing appears to reduce this difference between the two states.

The ρ_a values can also be obtained from the peak stress-temperature curves shown in Figure 7b. The so-obtained ρ_a values for the untreated fibre-matrix interface in the glassy state and rubbery state are $\rho_a|^{\text{glassy}}_{\text{untreated}} = 4.468 \times 10^8\ \text{J/m}^3$ and $\rho_a|^{\text{rubbery}}_{\text{untreated}} = 8.957 \times 10^8\ \text{J/m}^3$, respectively, while those for the treated fibre-matrix interface are $\rho_a|^{\text{glassy}}_{\text{treated}} = 4.501 \times 10^8\ \text{J/m}^3$ and $\rho_a|^{\text{rubbery}}_{\text{treated}} = 5.799 \times 10^8\text{J/m}^3$, respectively. These results suggest that: (1) the ρ_a value of the interfaces in the rubbery state is larger than the corresponding value in the glassy state; (2) the fibre sizing and the resulting covalent bonding between the fibre and the matrix has little effect on the ρ_a value of the interface in the glassy state, but it reduces the ρ_a value in the rubbery state.

With the above observations, the existence of a transition zone (i.e., 450 K to 520 K) in which the peak stress does not decrease linearly with temperature (see Figure 7b) may be explained as a result of the combined effect of changing $\frac{k_B}{v_a}\ln\left(\frac{2\dot{\varepsilon}}{\dot{\varepsilon}_0}\right)$ and ρ_a in this zone: the increase of the absolute value of the former with temperature leads to a decrease in the peak stress while the increase of the latter with temperature leads to an increase in the peak stress (see Eq. 1).

It is interesting to note that the slopes of the curves in the glassy state (–0.476 MPa/K and –0.475 MPa/K) are in good agreement with the experimental test results of epoxy which are in the range of –0.4359 to –0.4832 MPa/K [59]. This might be a coincidence considering the differences between the simulations and the tests: (1) the strain rate in the MD simulations is significantly higher than that in the tests, which generally leads to much higher peak stress for the former as is the case for the present study; (2) the peak stress of the epoxy may be considered to be slightly higher than that of the interface as informed by the failure morphologies of the models (Figures 3 and 5); (3) compared with the simulation models, the macroscopic specimens in the tests generally have more defects which may reduce their peak stress. Nevertheless, it is clear that the both the simulations and the tests exhibit a linear decreasing trend of the peak stress with the temperature for a specific temperature range. Furthermore, considering the two terms in the Eyring equation (i.e., $\frac{k_B}{v_a}\ln\left(\frac{2\dot{\varepsilon}}{\dot{\varepsilon}_0}\right)$ and ρ_a) which define the slope and the intercept of the peak stress-temperature curve, respectively, the similar experimental and simulation results in terms of the slope suggest that the strain rate might only have a small effect on the term $\frac{k_B}{v_a}\ln\left(\frac{2\dot{\varepsilon}}{\dot{\varepsilon}_0}\right)$ while having a significant effect on the ρ_a value. Therefore, when establishing a coupled thermal-mechanical multiscale

model, special attention should be paid to the apparent activation energy density as a function of strain rate (i.e., $\rho_a(\dot{\varepsilon})$).

3.4.2. Elastic Modulus

When the displacement is relatively small (e.g., <0.5 nm), the fibre-matrix interface remains almost intact and the displacement can be considered to be the same as the elongation of the matrix; as a result, the slope of the initial linear portion (i.e., $\varepsilon < 0.04$) of the stress-nominal strain curve (Figure 7a) may be taken as the elastic modulus of the matrix. It should, however, be noted that the so-obtained elastic modulus is not the same as Young's modulus, as periodic boundary conditions are applied in the *y* and *z* directions of the MD models and the interface/matrix is thus subjected to a uniaxial strain state (i.e., the strains in the *y* and *z* directions are equal to zero) (see Figures 8a and 8b). The so-obtained elastic moduli for the two models at different temperatures are shown in Figure 7c. Similar to the observations for the peak stress (Figure 7b), for both the untreated and sizing-treated models, the elastic modulus decreases almost linearly with temperature until T_g is reached, after which a plateau occurs with an almost constant elastic modulus for the temperature between 450 K and 520 K; when the temperature exceeds 520 K, the elastic modulus decreases again rapidly with temperature. It is evident from Figure 7c that the moduli of the untreated and sizing-treated fibre-matrix interfaces are almost identical at different temperatures before entering the rubbery state.

Figure 8c compares the simulation results with the experimentally obtained Young's modulus of epoxy at various temperatures reported in Ref.[60]. To make the comparison, the elastic moduli shown in Figure 8c for the uniaxial strain state ($E_{\text{uniaxial strain}}$) were first converted to Young's modulus (E_Y) using the following equation based on Hooke's Law [61]:

$$\sigma_{xx} = E_{\text{uniaxial strain}}\,\varepsilon_{xx} = \frac{E_Y(1-\nu)}{(1+\nu)(1-2\nu)}\varepsilon_{xx} \qquad (2)$$

In the conversion process, Poisson's ratio (ν) of the epoxy DGEBA/mPDA in the glassy state was chosen to be in the range from 0.3530 [62] to 0.4100 [63] based on the existing experimental studies. In the rubbery state, the Poisson's ratio is known to be close to 0.5 [64, 65], so it was chosen to be in the range from 0.4925 [66] to 0.4990. It is evident from Figure 8c that the experimental results fall well within the estimated range of the simulations for both the glassy and the rubbery states. It should, however, be noted that the simulation results are affected by the following factors: (1) the nonbonding and covalent bond interactions between the fibre and the matrix may have affected the mobility of surrounding molecules of the matrix; and (2) the strain rate in the simulations is significantly higher than that in the experiments. Nevertheless, the effect of (1) is believed to be small at least in the glassy state or for the interface without fibre sizing [67, 68], while the effect of strain rate on the elastic modulus is generally much less significant than that on the peak stress of epoxy resin [69-71]. Therefore, the comparison shown in Figure 8c, although may not be considered a rigorous quantitative verification, demonstrates the validity of the MD models in capturing the variation trend of elastic modulus with temperature.

The variation of elastic modulus with temperature (Figure 7c) may also be interpreted by the theory of thermodynamics. Based on elastic deformation, the tensile modulus E_t at a specific temperature T is given by [72]:

$$E_t = \frac{L}{A}\left(\frac{\partial f}{\partial L}\right)_T, \tag{3}$$

where L is the length of the sample, the cross-sectional area A is a constant for the uniaxial strain state, while isothermal tension f is given by [73]:

$$f = \left(\frac{\partial F}{\partial L}\right)_T = \left(\frac{\partial U}{\partial L}\right)_T - T\left(\frac{\partial S}{\partial L}\right)_T. \tag{4}$$

In Eq. 4, $F = U - TS$ is the Helmholtz free energy, U is the internal energy, S is the entropy. By combining Eqs. (3) and (4), the tensile modulus can be expressed as follows:

$$E_{\mathrm{t}} = \frac{L}{A}\left\{\frac{\partial}{\partial L}\left[\left(\frac{\partial U}{\partial L}\right)_T - T\left(\frac{\partial S}{\partial L}\right)_T\right]\right\} = \frac{1}{AL}\left[\left(\frac{\partial^2 U}{\partial \varepsilon^2}\right)_{T,A} - T\left(\frac{\partial^2 S}{\partial \varepsilon^2}\right)_{T,A}\right] = E_{\mathrm{U}} + E_{\mathrm{S}}. \tag{5}$$

Eq. 5 suggests that the tensile modulus is the sum of two components, E_{U} and E_{S}, which are derived from the responses of internal energy density (U/AL) and entropy density (S/AL) to changes in the strain, respectively, for a constant temperature [72, 74, 75]. The two components represent the energetic and entropic elasticity of the matrix, respectively.

It can also be derived from Eq. 5 that the term $-\frac{1}{AL}\left(\frac{\partial^2 S}{\partial \varepsilon^2}\right)_{T,A}$ defines the rate of change of the elastic modulus with temperature. Therefore, the results in Figure 7c indicate that in the glassy state, the values of $-\frac{1}{AL}\left(\frac{\partial^2 S}{\partial \varepsilon^2}\right)_{T,A}$ are –0.00676 GPa/K and –0.00637 GPa/K for the untreated and the treated interfaces, respectively, while in the rubbery state, the values for the former and the latter are –0.0131 GPa/K and –0.00841 GPa/K, respectively. It is not surprising that the rate of change is larger in the rubbery state than in the glassy state due to the greater entropic elasticity in the former. It may be explained by the differences between the two states in microscopic properties such as the mobility or freedom of the molecules, which result in different macroscopic mechanical properties in a statistical sense.

In addition, the rate of change for the treated interface is smaller than that of the untreated interface when the temperature is higher than 520 K (Figure 7c). This is believed to be due to the fibre sizing in the former which enhances the covalent bonds at the interface and thus limits the mobility of the surrounding molecules and reduces the entropy. As a result, in the rubbery state, the contribution of entropy elasticity to the modulus of the sizing-treated fibre-matrix interface is significantly smaller than that in the untreated interface.

Furthermore, Eq. 5 suggests that the term $\frac{1}{AL}\left(\frac{\partial^2 U}{\partial \varepsilon^2}\right)_{T,A}$ or E_{U} (the contribution of the energetic elasticity to the modulus) may be found as the longitudinal intercepts (i.e., when $T = 0$) of the lines in Figure 7c. By doing so, it can be derived that E_{U} increases when the temperature increases from T_{g} to around 520 K. The elastic moduli shown in Figure 7c are a result of the combined effect of the increasing E_{U} and the decreasing E_{S} when the matrix changes from the glassy state to the rubbery state. This explains the existence of a plateau of modulus in the transition zone (450 K – 520 K) due to the competition between the energetic and entropic elasticity.

3.4.3. Interfacial Toughness

The interfacial toughness or the practical work of adhesion is defined as the total mechanical energy G required to break a bond [76-78] and can be calculated as the area surrounded by the stress-displacement curve and the two axes (i.e., stress axis and displacement axis). Figure 9 shows the interfacial toughness of the untreated (yellow dots) and sizing-treated (blue dots) fibre-matrix interfaces at different temperatures. The toughness of the untreated interface is insensitive to temperature before entering the rubbery state, ranging from 0.256 J/m^2 to 0.321 J/m^2, while it decreases from 0.331 J/m^2 to 0.244 J/m^2 when the temperature decreases from 560 K to 600 K. These observations are consistent with the previous experimental results on the Mode I fracture toughness of epoxy [79]. By contrast, the toughness of the treated interface is almost an order of magnitude larger than that of the former and appears more sensitive to temperature; four distinct stages can be seen form Figure 9: (1) from 300 K to 380 K, the toughness increases with temperature; (2) from 380 K to T_g, the toughness decreases with temperature; (3) from T_g to 520 K, the toughness plateaus; and (4) the toughness decreases rapidly after the temperature exceeds 520 K. In other words, the existence of covalent bonds provided by the silane grafted on the fibre at the interface makes the toughness sensitive to temperature.

3.4.4. Summary

The analysis and discussions presented above clarify the patterns of variation in the mechanical properties of the two interfaces over a wide range of temperatures. Importantly, the thermal-mechanical effects on the peak stress, elastic modulus, toughness as well as the parameters defining their variations with temperature [i.e., ρ_a, E_U, $\frac{k_B}{v_a}\ln\left(\frac{2\dot{\varepsilon}}{\dot{\varepsilon}_0}\right)$ and $-\frac{1}{AL}\left(\frac{\partial^2 S}{\partial \varepsilon^2}\right)_{T,A}$] are quantified. Furthermore, the effects of sizing on the above properties and parameters of the interface are also clarified and quantified. These parameters are important for the understanding of thermal-mechanical coupling problems and may be used in future development of multiscale and multifield coupling models. For instance, the peak stress, elastic modulus, and toughness can be used to verify the coarse-grained (CG) models; the parameters defining their variations with temperature may contribute to establishing a thermal-mechanical model of the interface that can be used for finite element analysis.

3.5. Deterioration Mechanism of Fibre-Matrix Interfaces under Coupled Thermal-Mechanical Actions

MD simulations offer an atomistic view of the failure process and have been used remarkably successfully to clarify the underlying physics of the probabilistic models for life prediction [80, 81]. The ReaxFF MD simulations conducted in this study allow the breakage/formation of covalent bonds to be examined. The relaxation time of the thermal-mechanical process is comparable to most MD studies (e.g., on thermal decomposition [82] or on pull-out-induced chemical bond breaking [83]), and is sufficient to reflect the degradation of the chemical bonds inside the matrix under coupled thermal-mechanical effects. It was found that the C-O bond (ether linkage, see Figure 10a) in the polymer is the main broken bond during the debonding process of both interface models. For the treated fibre-matrix interface, the Si-O bond between the fibre and the silane remains intact even after complete debonding. Figure 10b shows the total amount of the C-O bond that has broken (referred to as breakage amount hereafter) after complete debonding of the

untreated interface and sizing-treated interfaces at temperatures ranging from 300 K ~ 600 K. It is obvious that the breakage amount of the treated interface is significantly larger than that of the untreated interface due to the larger displacement of the former. The breakage amount of the untreated interface increases almost linearly with temperature until T_g, while for the treated interface, the linear increase of the breakage amount only occurs when the temperature is below 380 K after which the rate of increase becomes significantly smaller until T_g. At temperatures above T_g, the breakage amounts of both interfaces do not change much with the temperature.

To clarify the process of covalent bond breaking, the breakage amount (N_b) of the C-O bond is plotted against the debonding displacement (D) and temperature for the two interfaces in Figures 10c and 10d, respectively. In addition, several isolines, each representing the same breakage amount, are plotted in each figure. By observing the isolines, it is evident that the lifetime of the C-O bond (i.e., $\tau = \Delta t/\Delta N_b = \Delta D/\Delta N_b V$, where V is the tensile velocity) decreases with temperature for both interfaces. To estimate the lifetime of the C-O bond at different temperatures, the breakage amount is further plotted against displacement in Figure 11a for both interfaces. In Figure 11a, the data points are only for relatively small displacements and thus relatively small breakage amount ($\leq 2\%$), as otherwise the configuration of the molecular chains within the matrix may be significantly affected by plastic deformation, and the strain state within the matrix may become nonuniform. It is evident from Figure 11a that, for both interfaces at a specific temperature, the breakage amount increases nearly linearly with the displacement, suggesting that the fracture mechanism of the C-O bond at the initial stage does not change in a statistical sense.

Figures 11b and 11c show the estimated lifetime of the C-O bond for the two interfaces based on the data in Figure 11a and the equation $\tau = \Delta D/\Delta N_b V$. It can be seen that the lifetime derived from different data points (i.e., different breakage amounts) at the same temperature is nearly the same for both interfaces. The results on the lifetime may also be examined with reference to the kinetic theory which can be expressed by [84]:

$$\tau = \tau_0 \exp\left[\frac{\Delta E(\dot{\varepsilon}; E_b)}{k_B T}\right], \tag{6}$$

where $1/\tau_0$ is the intrinsic frequency of the chemical bond (e.g., $1/\tau_0 \approx 3.77 \times 10^{13}$ Hz for the C-O bond [85]), and $\Delta E(\dot{\varepsilon}; E_b)$ is the activation energy of the current chemical bond (i.e., C-O bond) and is a function of the strain rate $\dot{\varepsilon}$, with the bond energy E_b as a parameter. By using Eq. 6 to fit the simulation results, the activation energies under tension can be obtained, as shown in Figures 11b and 11c. The so-obtained activation energies of the C-O bond are 7.85 kJ/mol at relatively low temperatures (i.e., <380 K) in the glassy state and 5.15 kJ/mol at relatively high temperatures (i.e., >480 K) in the rubbery state at the untreated interface, while they are 7.55 kJ/mol (glassy state) and 4.85 kJ/mol (rubbery state) at the sizing-treated interface. It is not surprising that the activation energies of the two models are close due to the use of the same matrix material and boundary conditions in both models. It is also noted that there is a significant difference (i.e., 2.70 kJ/mol) between the activation energies in the glassy and rubbery states. In addition, for both interfaces, there is a transition region (i.e., 380 K ~ 480 K) in which the simulation data points fall between the two theoretical curves defined by the two abovementioned activation energies of each interface. As the activation energy $\Delta E(\dot{\varepsilon}; E_b)$ is an indicator of the

mechanism of chemical bond breakage [86], the results shown in Figures 11b and 11c suggest that when doing accelerated exposures tests on FRP composites with the fibre and the matrix materials adopted in this study, the temperature should not exceed 380 K.

The results presented above are important for the design and interpretation (e.g., deterioration mechanism and lifetime of chemical bonds) of the accelerated exposure tests on FRP composites and have not been quantified in any existing studies to the best of the authors' knowledge. In addition, the activation energy $\Delta E(\dot{\varepsilon}; E_{\mathrm{b}})$ of the C-O bond in the glass and rubber states may be used for multiscale modelling of deterioration of FRP composites under coupled thermal-mechanical actions. In terms of the time scale of degradation, the relationship between the activation energy $\Delta E(\dot{\varepsilon}; E_{\mathrm{b}})$ and the boost potential [87, 88] of the degradation process under coupled thermal-mechanical action can be further clarified in the future. In this way, the physical time corresponding to the macroscopic deterioration process can be obtained by multiplying the MD time with the corresponding acceleration factor [87, 88], thus establishing a link between the time scale of the MD result and the macroscopic behaviour. Furthermore, although the present study is on fibre-matrix interfaces, the properties derived from the C-O bond in the matrix are also valid for use in future studies on the durability of epoxy materials.

4. CONCLUSIONS

This paper has presented a study on the properties and deterioration mechanism of fibre-matrix interfaces under tension at various temperatures using ReaxFF MD simulations. Two interface models were established to investigate the effects of fibre sizing which significantly enhances the covalent bonds between the fibre and the matrix. The MD simulations were performed over a wide range of temperatures from 300 K~ 600 K to cover both the glassy and the rubbery states of the polymeric matrix. The study involves investigations into the glass transition temperature (T_{g}), the stress-displacement curves and key mechanical properties, the morphologies and characteristics in the debonding process, as well as the deterioration mechanism of chemical bonds based on the simulation results. The results and discussions presented above allow the following conclusions to be drawn:

(1) The MD models developed in this study are capable of accurate prediction of T_{g} of the matrix. The predicted T_{g} (i.e., 450 K) is in good agreement with the existing experimental result of epoxy with the same monomer (DGEBA) and curing agent (mPDA), suggesting that the thermal mobility of the molecules in the simulations is close to that in real cases.
(2) The debonding process is characterized by three types of motions, namely, cavitation/nucleation, plastic yield, and bridge rupture. The covalent bonds provided by the fibre sizing can significantly increase the plastic flow, forming plastic plateaus up to 5~6 nm and maintaining bridges up to lengths of over 24 nm. After bridge rupture, the amount of residual matrix tends to rise with the temperature, and approximately 25 to 80 times more residual matrix was found on the treated fibre surfaces than on the untreated fibre surfaces.
(3) The fibre sizing does not have a significant effect on the debonding process in the initial stage up to the peak stress of the interface. Afterwards, the chemical bonds provided by the fibre

sizing start to protect the interface from separation: the debonding ratio is in the range of 50% to 80% at the displacement of 3 nm for the sizing-treated interface, whereas for the untreated interface, the debonding ratio is already approximately 90% to 95% at 2 nm.

(4) The peak stresses of the untreated and sizing-treated fibre-matrix interfaces are nearly equal and both decrease almost linearly with increasing temperature in the glassy state. For both interfaces, the peak stress then somewhat plateaus from T_g to 520 K, after which the peak stress decreases again almost linearly with temperature. The rate of decrease in the last stage (i.e., >520 K) is significantly higher than that in the glassy state. The simulated variation of peak stress with temperature is consistent with the previous experimental tests on epoxy. With reference to Eyring's theory, the key parameters of the interfaces including the activation energy density ρ_a and the slope of the peak stress-temperature curve $\frac{k_B}{v_a}\ln\left(\frac{2\dot{\varepsilon}}{\dot{\varepsilon}_0}\right)$ are quantified. It was also found that ρ_a may be more sensitive to strain rates than $\frac{k_B}{v_a}\ln\left(\frac{2\dot{\varepsilon}}{\dot{\varepsilon}_0}\right)$.

(5) The trend of variation of elastic modulus of the matrix with temperature is similar to that for the interfacial peak stress for both interfaces. The modulus decreases more rapidly in the rubbery state than in the glassy state due to the greater entropic elasticity in the former. Young's moduli obtained from the simulations for various temperatures are in good agreement with previous experimental results. With reference to the theory of thermodynamics, the contributions of the energetic and entropic elasticity to the elastic modulus are clarified and quantified.

(6) The toughness of the untreated interface is insensitive to temperature before entering the rubbery state, while from 560 K to 600 K, a decrease in toughness was observed. These properties are consistent with previous experimental results on epoxy resin. By contrast, the toughness of the sizing-treated interface is almost an order of magnitude larger than that of the untreated interface and is more sensitive to temperature.

(7) The breakage amount of the C-O bonds is larger in the treated interface than in the untreated interface due to the larger debonding displacement of the former. Informed by the relationship between the breakage amount and the displacement, the lifetime of the C-O bond under various temperatures was derived. The so-obtained lifetime was then used with the kinetic theory to obtain the activation energies $\Delta E(\dot{\varepsilon}; E_b)$ for the C-O bond at various temperatures. By using the activation energies as an indicator of the deterioration mechanism, it was found that the temperature for the accelerated exposure tests of FRP composites using the materials of this study should not exceed 380 K to ensure that the fundamental deterioration mechanism is not changed by the increasing temperature.

This study provides significant insights into the fundamental deterioration mechanism of the fibre-matrix interface under coupled thermal-mechanical actions by performing debonding simulations at temperatures from 300 K to 600 K. It demonstrates that Eyring's theory, which has been widely adopted for polymers, is also applicable to the behaviour of interfacial debonding. Importantly, in this study, several key properties of the interfaces and key parameters affecting the debonding process have been quantified; these properties/parameters shed light on the design and interpretation of accelerated exposure tests and may be used in future multiscale modelling of the durability of FRP composites.

ACKNOWLEDGEMENTS

The authors gratefully acknowledge the financial support provided by the Hong Kong Research Grants Council (Project No: T22-502/18-R).

REFERENCES

[1] Masuelli M A, *Introduction of fibre-reinforced polymers− polymers and composites: concepts, properties and processes*, in *Fiber reinforced polymers-the technology applied for concrete repair*. 2013, IntechOpen.

[2] Teng J G, Chen J F, Smith S T, Lam L, *FRP-strengthened RC structures*. 2002, New York: Wiley.

[3] Di Pasquale G, Motto O, Rocca A, Carter J T, McGrail P T, Acierno D. New high-performance thermoplastic toughened epoxy thermosets. Polymer 1997; 38(17): 4345-4348.

[4] Frollini E, Silva C G, Ramires E C, *2 - Phenolic resins as a matrix material in advanced fiber-reinforced polymer (FRP) composites*, in *Advanced Fibre-Reinforced Polymer (FRP) Composites for Structural Applications*, J. Bai, Editor. 2013, Woodhead Publishing. p. 7-43.

[5] Zhao Y-P, *Physical Mechanics of Surfaces and Interfaces*. 2012, Beijing: Science Press.

[6] Buehler M J, Wong S Y. Entropic elasticity controls nanomechanics of single tropocollagen molecules. Biophys J 2007; 93(1): 37-43.

[7] Thwe M M, Liao K. Durability of bamboo-glass fiber reinforced polymer matrix hybrid composites. Compos Sci Technol 2003; 63(3): 375-387.

[8] Karbhari V, Chin J, Hunston D, Benmokrane B, Juska T, Morgan R, . . . Reynaud. Durability gap analysis for fiber-reinforced polymer composites in civil infrastructure. J Compos Constr 2003; 7(3): 238-247.

[9] Hristozov D, Wroblewski L, Sadeghian P. Long-term tensile properties of natural fibre-reinforced polymer composites: Comparison of flax and glass fibres. Compos B Eng 2016; 95: 82-95.

[10] Panaitescu I, Koch T, Archodoulaki V-M. Accelerated aging of a glass fiber/polyurethane composite for automotive applications. Polym Test 2019; 74: 245-256.

[11] Bazli M, Zhao X-L, Jafari A, Ashrafi H, Raman R S, Bai Y, Khezrzadeh H. Durability of glass-fibre-reinforced polymer composites under seawater and sea-sand concrete coupled with harsh outdoor environments. Adv Struct Eng 2021; 24(6): 1090-1109.

[12] Laidler K J. The development of the Arrhenius equation. J Chem Educ 1984; 61(6): 494.

[13] Sousa J M, Correia J R, Cabral-Fonseca S, Diogo A C. Effects of thermal cycles on the mechanical response of pultruded GFRP profiles used in civil engineering applications. Compos Struct 2014; 116: 720-731.

[14] Selzer R, Friedrich K. Mechanical properties and failure behaviour of carbon fibre-reinforced polymer composites under the influence of moisture. Compos Part A-Appl S 1997; 28(6): 595-604.

[15] Sun P, Zhao Y, Luo Y, Sun L. Effect of temperature and cyclic hygrothermal aging on the interlaminar shear strength of carbon fiber/bismaleimide (BMI) composite. Mater Des 2011; 32(8-9): 4341-4347.
[16] Grammatikos S A, Jones R G, Evernden M, Correia J R. Thermal cycling effects on the durability of a pultruded GFRP material for off-shore civil engineering structures. Compos Struct 2016; 153: 297-310.
[17] Azwa Z, Yousif B, Manalo A, Karunasena W. A review on the degradability of polymeric composites based on natural fibres. Mater Des 2013; 47: 424-442.
[18] Kinloch A, Shaw S, Tod D, Hunston D. Deformation and fracture behaviour of a rubber-toughened epoxy: 1. Microstructure and fracture studies. Polymer 1983; 24(10): 1341-1354.
[19] Truss R, Clarke P, Duckett R, Ward I. The dependence of yield behavior on temperature, pressure, and strain rate for linear polyethylenes of different molecular weight and morphology. Journal of Polymer Science: Polymer Physics Edition 1984; 22(2): 191-209.
[20] Ree T, Eyring H. Theory of non-newtonian flow. i. solid plastic system. J Appl Phys 1955; 26(7): 793-800.
[21] Bauwens-Crowet C, Bauwens J C, Homes G. Tensile yield-stress behavior of glassy polymers. Journal of Polymer Science Part A-2: Polymer Physics 1969; 7(4): 735-742.
[22] Mayr A E, Cook W D, Edward G H. Yielding behaviour in model epoxy thermosets—I. Effect of strain rate and composition. Polymer 1998; 39(16): 3719-3724.
[23] Gent A, Petrich R. Adhesion of viscoelastic materials to rigid substrates. Proceedings of the Royal Society of London. A. Mathematical and Physical Sciences 1969; 310(1502): 433-448.
[24] Kim K-Y, Ye L. Interlaminar fracture toughness of CF/PEI composites at elevated temperatures: roles of matrix toughness and fibre/matrix adhesion. Compos Part A-Appl S 2004; 35(4): 477-487.
[25] Martyniuk K, Sørensen B F, Modregger P, Lauridsen E M. 3D in situ observations of glass fibre/matrix interfacial debonding. Compos Part A-Appl S 2013; 55: 63-73.
[26] De Luca F, Sernicola G, Shaffer M S, Bismarck A. "Brick-and-Mortar" nanostructured interphase for glass-fiber-reinforced polymer composites. ACS Appl Mater Interfaces 2018; 10(8): 7352-7361.
[27] LLorca J, González C, Molina-Aldareguía J M, Segurado J, Seltzer R, Sket F, . . . Canal L P. Multiscale modeling of composite materials: a roadmap towards virtual testing. Adv Mater 2011; 23(44): 5130-5147.
[28] Gao J, Shakoor M, Domel G, Merzkirch M, Zhou G, Zeng D, . . . Liu W K. Predictive multiscale modeling for Unidirectional Carbon Fiber Reinforced Polymers. Compos Sci Technol 2020; 186: 107922.
[29] Yeon J, van Duin A C T, Kim S H. Effects of Water on Tribochemical Wear of Silicon Oxide Interface: Molecular Dynamics (MD) Study with Reactive Force Field (ReaxFF). Langmuir 2016; 32(4): 1018-1026.

[30] Bhati M, Nguyen Q A, Biswal S L, Senftle T P. Combining ReaxFF Simulations and Experiments to Evaluate the Structure–Property Characteristics of Polymeric Binders in Si-Based Li-Ion Batteries. ACS Appl Mater Interfaces 2021; 13(35): 41956-41967.
[31] Yaphary Y L, Yu Z, Lam R H W, Hui D, Lau D. Molecular dynamics simulations on adhesion of epoxy-silica interface in salt environment. Compos B Eng 2017; 131: 165-172.
[32] Xiao Y, Xian G. Effects of moisture ingress on the bond between carbon fiber and epoxy resin investigated with molecular dynamics simulation. Polymer Composites 2018; 39(S4): E2074-E2083.
[33] Wang X Q, Lau D. Atomistic investigation of GFRP composites under chloride environment. Adv Struct Eng 2021; 24(6): 1138-1149.
[34] Benmokrane B, Hassan M, Robert M, Vijay P V, Manalo A. Effect of Different Constituent Fiber, Resin, and Sizing Combinations on Alkaline Resistance of Basalt, Carbon, and Glass FRP Bars. J Compos Constr 2020; 24(3): 04020010.
[35] Lin K, Yu T. Debonding simulation of fibre-matrix interfaces of FRP composites with reactive force field. Construction and Building Materials 2021; 312: 125304.
[36] Plimpton S. Fast parallel algorithms for short-range molecular dynamics. J Comput Phys 1995; 117(1): 1-19.
[37] Bai C, Liu L, Sun H. Molecular dynamics simulations of methanol to olefin reactions in HZSM-5 zeolite using a ReaxFF force field. J Phys Chem C 2012; 116(12): 7029-7039.
[38] Steinbach P J, Brooks B R. New spherical-cutoff methods for long-range forces in macromolecular simulation. J Comput Chem 1994; 15(7): 667-683.
[39] Li Z F, Ruckenstein E. Strong Adhesion and Smooth Conductive Surface via Graft Polymerization of Aniline on a Modified Glass Fiber Surface. J Colloid Interface Sci 2002; 251(2): 343-349.
[40] Unger R, Braun U, Fankhänel J, Daum B, Arash B, Rolfes R. Molecular modelling of epoxy resin crosslinking experimentally validated by near-infrared spectroscopy. Comp Mater Sci 2019; 161: 223-235.
[41] Jesionowski T, Krysztafkiewicz A. Influence of silane coupling agents on surface properties of precipitated silicas. Appl Surf Sci 2001; 172(1-2): 18-32.
[42] Howarter J A, Youngblood J P. Optimization of Silica Silanization by 3-Aminopropyltriethoxysilane. Langmuir 2006; 22(26): 11142-11147.
[43] Chen W Y, Wang Y Z, Kuo S W, Huang C F, Tung P H, Chang F C. Thermal and dielectric properties and curing kinetics of nanomaterials formed from poss-epoxy and meta-phenylenediamine. Polymer 2004; 45(20): 6897-6908.
[44] Babayevsky P G, Gillham J. Epoxy thermosetting systems: dynamic mechanical analysis of the reactions of aromatic diamines with the diglycidyl ether of bisphenol A. J Appl Polym Sci 1973; 17(7): 2067-2088.

[45] Chen W-Y, Wang Y-Z, Kuo S-W, Huang C-F, Tung P-H, Chang F-C. Thermal and dielectric properties and curing kinetics of nanomaterials formed from poss-epoxy and meta-phenylenediamine. Polymer 2004; 45(20): 6897-6908.
[46] Morita H, Tanaka K, Kajiyama T, Nishi T, Doi M. Study of the Glass Transition Temperature of Polymer Surface by Coarse-Grained Molecular Dynamics Simulation. Macromolecules 2006; 39(18): 6233-6237.
[47] Zhou J, Lucas J P. Hygrothermal effects of epoxy resin. Part II: variations of glass transition temperature. Polymer 1999; 40(20): 5513-5522.
[48] Frankland S J V, Harik V M, Odegard G M, Brenner D W, Gates T S. The stress–strain behavior of polymer–nanotube composites from molecular dynamics simulation. Compos Sci Technol 2003; 63(11): 1655-1661.
[49] Elkhateeb M G, Shin Y C. Molecular dynamics-based cohesive zone representation of Ti6Al4V/TiC composite interface. Mater Des 2018; 155: 161-169.
[50] Bank L C, Gentry T R, Thompson B P, Russell J S. A model specification for FRP composites for civil engineering structures. Constr Build Mater 2003; 17(6): 405-437.
[51] Subramaniyan A K, Sun C T. Continuum interpretation of virial stress in molecular simulations. Int J Solids Struct 2008; 45(14): 4340-4346.
[52] Campo E A, *3 - Thermal Properties of Polymeric Materials*, in *Selection of Polymeric Materials*, E.A. Campo, Editor. 2008, William Andrew Publishing: Norwich, NY. p. 103-140.
[53] Baljon A R, Robbins M O. Energy dissipation during rupture of adhesive bonds. Science 1996; 271(5248): 482-484.
[54] Kausch H-H, *Polymer fracture*. Vol. 2. 2012: Springer Science & Business Media.
[55] Eyring H. Viscosity, plasticity, and diffusion as examples of absolute reaction rates. J Chem Phys 1936; 4(4): 283-291.
[56] Roetling J. Yield stress behaviour of polymethylmethacrylate. Polymer 1965; 6(6): 311-317.
[57] Van Breemen L C, Engels T A, Klompen E T, Senden D J, Govaert L E. Rate-and temperature-dependent strain softening in solid polymers. J Polym Sci, Part B: Polym Phys 2012; 50(24): 1757-1771.
[58] Wang J, Wang W, Liu Y, Bai H. Characterization of activation energy for flow in metallic glasses. Physical Review B 2011; 83(1): 012201.
[59] Banea M, De Sousa F, Da Silva L, Campilho R, de Pereira A B. Effects of temperature and loading rate on the mechanical properties of a high temperature epoxy adhesive. J Adhes Sci Technol 2011; 25(18): 2461-2474.
[60] Essmeister J, Taublaender M J, Koch T, Cerrón-Infantes D A, Unterlass M M, Konegger T. High modulus polyimide particle-reinforcement of epoxy composites. Materials Advances 2021; 2(7): 2278-2288.
[61] Liu J, Chen Z, Elsworth D, Miao X, Mao X. Linking gas-sorption induced changes in coal permeability to directional strains through a modulus reduction ratio. International Journal of Coal Geology 2010; 83(1): 21-30.

[62] Rao V, Drzal L T. The dependence of interfacial shear strength on matrix and interphase properties. Polym Compos 1991; 12(1): 48-56.
[63] Drzal L T. The effect of polymeric matrix mechanical properties on the fiber-matrix interfacial shear strength. Materials Science and Engineering: A 1990; 126(1-2): 289-293.
[64] Plepys A, Farris R. Evolution of residual stresses in three-dimensionally constrained epoxy resins. Polymer 1990; 31(10): 1932-1936.
[65] Greaves G N, Greer A, Lakes R S, Rouxel T. Poisson's ratio and modern materials. Nature materials 2011; 10(11): 823-837.
[66] O'Brien D J, Sottos N, White S R. Cure-dependent viscoelastic Poisson's ratio of epoxy. Experimental mechanics 2007; 47(2): 237-249.
[67] Pozuelo J, Baselga J. Glass transition temperature of low molecular weight poly(3-aminopropyl methyl siloxane). A molecular dynamics study. Polymer 2002; 43(22): 6049-6055.
[68] Liu J, Wu Y, Shen J, Gao Y, Zhang L, Cao D. Polymer–nanoparticle interfacial behavior revisited: A molecular dynamics study. Physical Chemistry Chemical Physics 2011; 13(28): 13058-13069.
[69] Hsiao H, Daniel I M. Strain rate behavior of composite materials. Compos B Eng 1998; 29(5): 521-533.
[70] Fard M Y, Liu Y, Chattopadhyay A. Characterization of epoxy resin including strain rate effects using digital image correlation system. Journal of Aerospace Engineering 2012; 25(2): 308-319.
[71] Odegard G M, Jensen B D, Gowtham S, Wu J, He J, Zhang Z. Predicting mechanical response of crosslinked epoxy using ReaxFF. Chem Phys Lett 2014; 591: 175-178.
[72] Finn C B, *Thermal physics*. 2017: CRC Press.
[73] Ward I M, Sweeney J, *Mechanical properties of solid polymers*. 2012: John Wiley & Sons.
[74] Matsuoka S. Free volume, excess entropy and mechanical behavior of polymeric glasses. Polym Eng Sci 1981; 21(14): 907-921.
[75] Oleinik E F. Epoxy-aromatic amine networks in the glassy state structure and properties. Epoxy resins and composites IV 1986: 49-99.
[76] Volinsky A A, Moody N R, Gerberich W W. Interfacial toughness measurements for thin films on substrates. Acta Mater 2002; 50(3): 441-466.
[77] Lin K, Zhao Y-P. Mechanical peeling of van der Waals heterostructures: Theory and simulations. Extreme Mechanics Letters 2019; 30: 100501.
[78] Wei Z, Lin K, Wang X, Zhao Y-P. Peeling of graphene/molybdenum disulfide heterostructure at different angles: A continuum model with accommodations for van der Waals interaction. Compos Part A-Appl S 2021; 150: 106592.
[79] Banea M, Silva L d, Campilho R. Effect of temperature on tensile strength and mode I fracture toughness of a high temperature epoxy adhesive. J Adhes Sci Technol 2012; 26(7): 939-953.

[80] Zhang Z, Xu Z. Failure life prediction for carbon nanotubes. J Mech Phys Solids 2022; 164: 104907.
[81] Wang S, Shi J, Shimizu T, Xu J, Xu Z. Two-step heat fusion kinetics and mechanical performance of thermoplastic interfaces. Scientific Reports 2022; 12(1): 5701.
[82] Han S-p, Van Duin A C, Goddard III W A, Strachan A. Thermal decomposition of condensed-phase nitromethane from molecular dynamics from ReaxFF reactive dynamics. J Phys Chem B 2011; 115(20): 6534-6540.
[83] Chowdhury S C, Okabe T. Computer simulation of carbon nanotube pull-out from polymer by the molecular dynamics method. Compos Part A-Appl S 2007; 38(3): 747-754.
[84] Zhurkov S N. Kinetic concept of the strength of solids. Int J Fracture Mech 1965; 1(4): 311-323.
[85] Lin M S, Wang M W, Lee C T, Shao S Y. Accelerated ageing behavior of compatible IPNs based on epoxy and methacrylated epoxy resins. Polym Degrad Stab 1998; 60(2-3): 505-510.
[86] Beyer M K, Clausen-Schaumann H. Mechanochemistry: the mechanical activation of covalent bonds. Chem Rev 2005; 105(8): 2921-2948.
[87] Voter A F. Hyperdynamics: Accelerated Molecular Dynamics of Infrequent Events. Phys Rev Lett 1997; 78(20): 3908-3911.
[88] Chakraborty S, Zhang J, Ghosh S. Accelerated molecular dynamics simulations for characterizing plastic deformation in crystalline materials with cracks. Comp Mater Sci 2016; 121: 23-34.

FIGURES

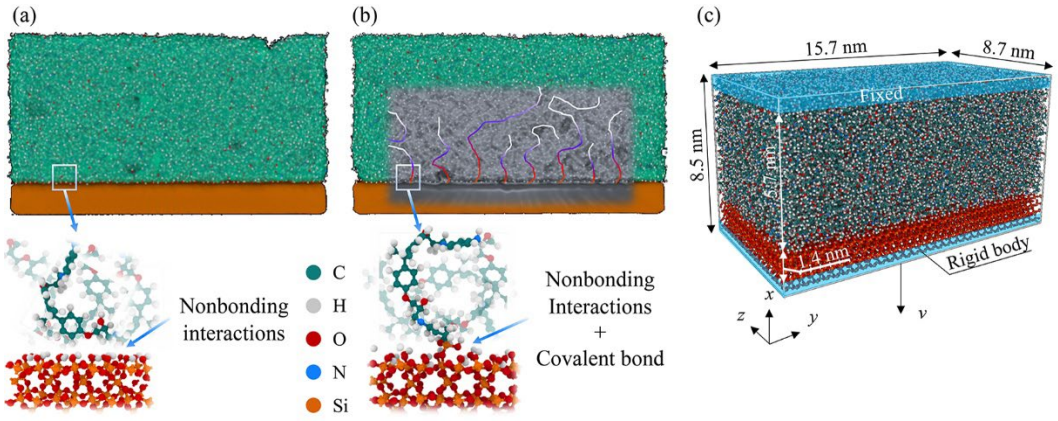

Figure 1. (a) Untreated fibre-matrix interface; (b) sizing-treated (grafted silanes) fibre-matrix interface; and (c) initial MD model before tension process.

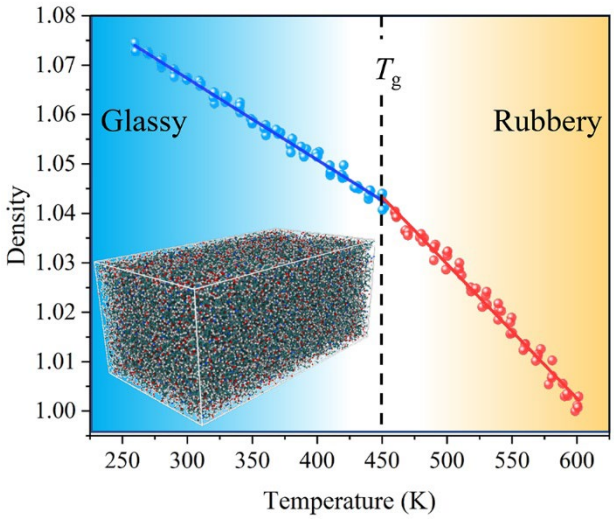

Figure 2. The dimensionless density of the matrix (epoxy resin) as a function of temperature.

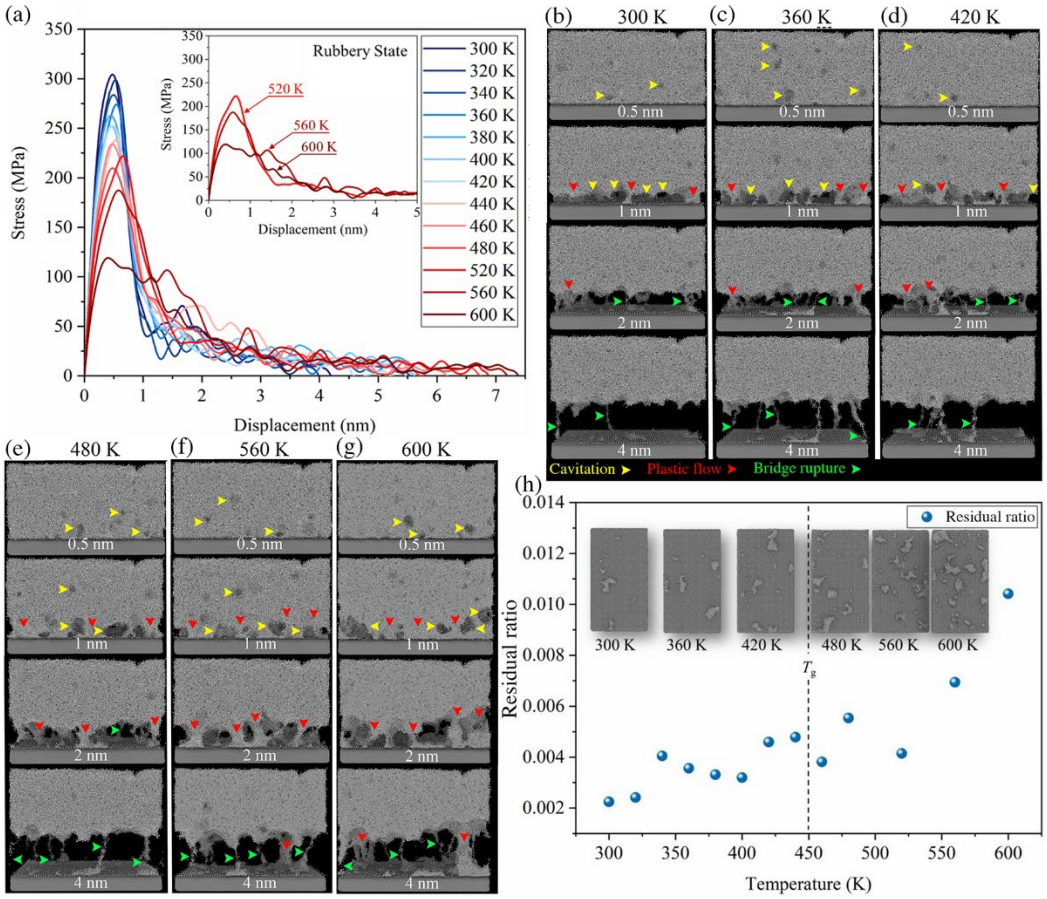

Figure 3. (a) Stress-displacement curves of the untreated fibre-matrix interface at different temperatures; (b-g) snapshots of the untreated fibre-matrix interface at different debonding distances and different temperatures (brighter regions show the matrix, darker regions show the fibre, the coloured arrows point to the locations where visible cavitation (yellow), plastic flow (red) and bridge rupture (green) occur.); and (h) residual ratio of the matrix on the fibre surface after debonding as a function of temperature, with the inserts showing representative snapshots.

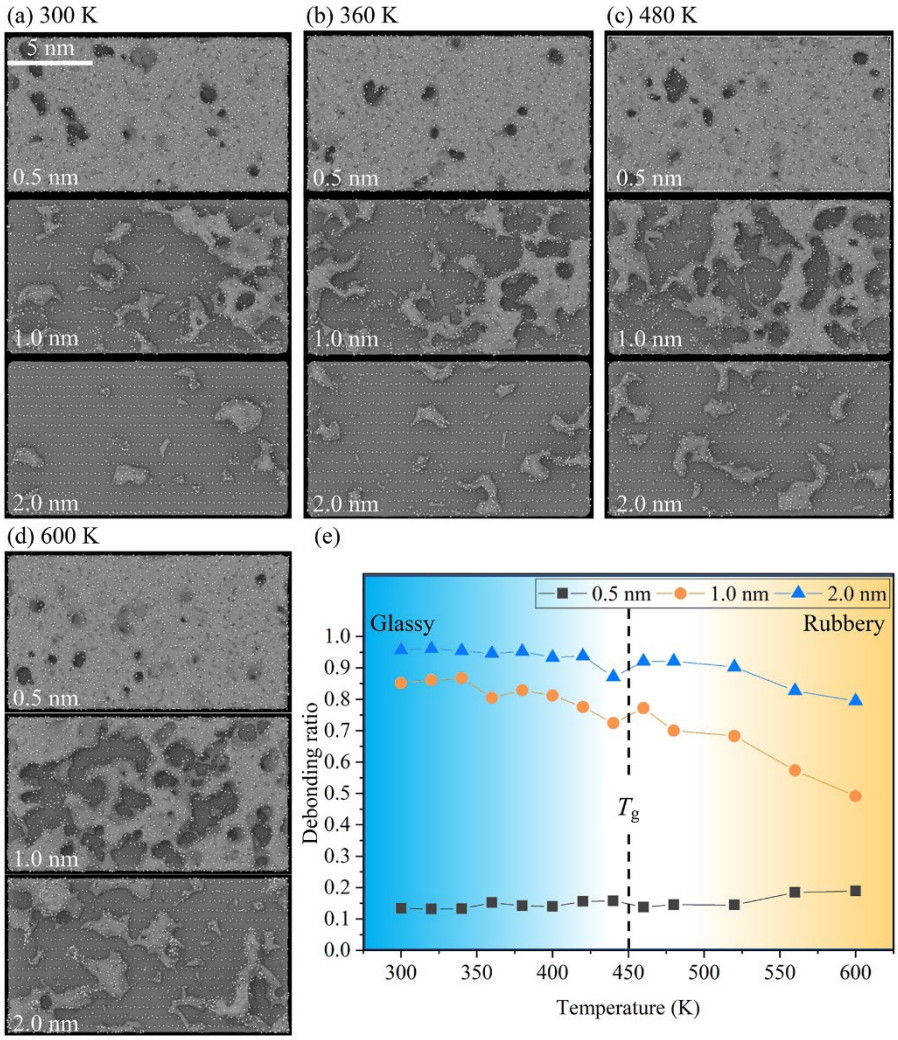

Figure 4. (a-d) Morphological evolution of the nonbonding interaction zone at the untreated fibre-matrix interface at different debonding distances and different temperatures; (e) Debonding ratio of the nonbonding interaction zone at different debonding distances as a function of temperature.

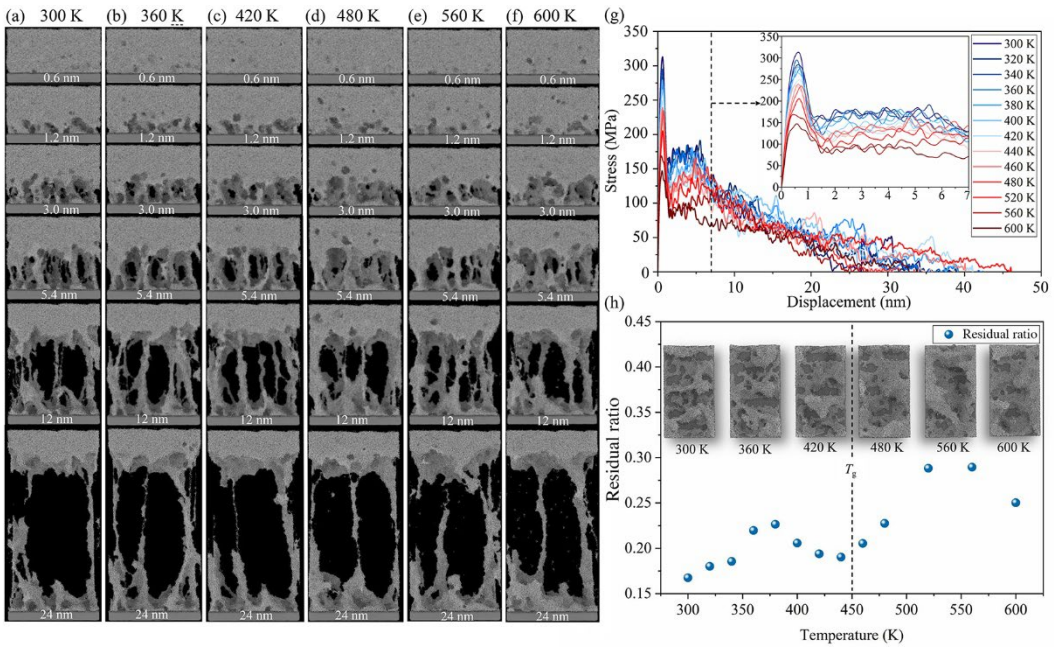

Figure 5. (a)-(f) Snapshots of the treated fibre-matrix interface at different debonding distances and different temperatures; (g) stress-displacement curves of the treated fibre-matrix interface at different temperatures; and (h) residual ratio of the matrix on the fibre surface after debonding as a function of temperature, with inserts showing representative snapshots.

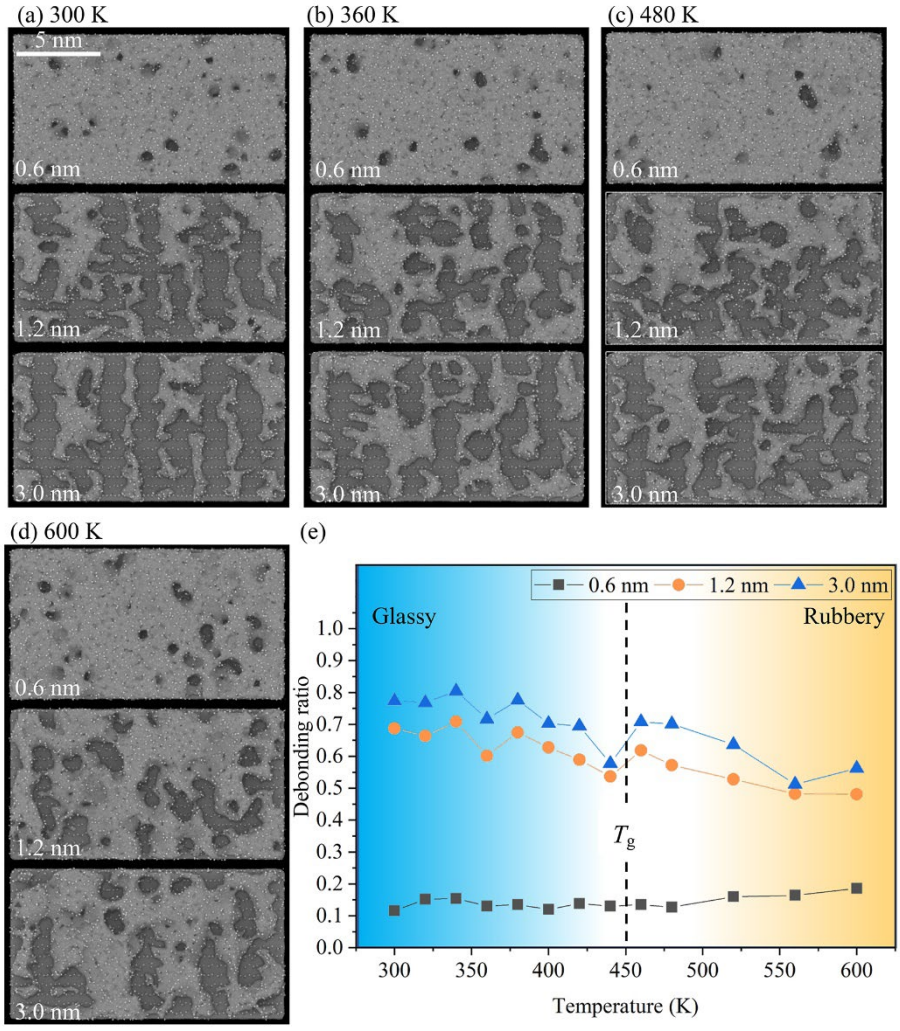

Figure 6. (a-d) Morphological evolution of the nonbonding interaction zone at the sizing-treated fibre-matrix interface at different debonding distances and different temperatures; (e) debonding ratio of the nonbonding interaction zone at different debonding distances as a function of temperature.

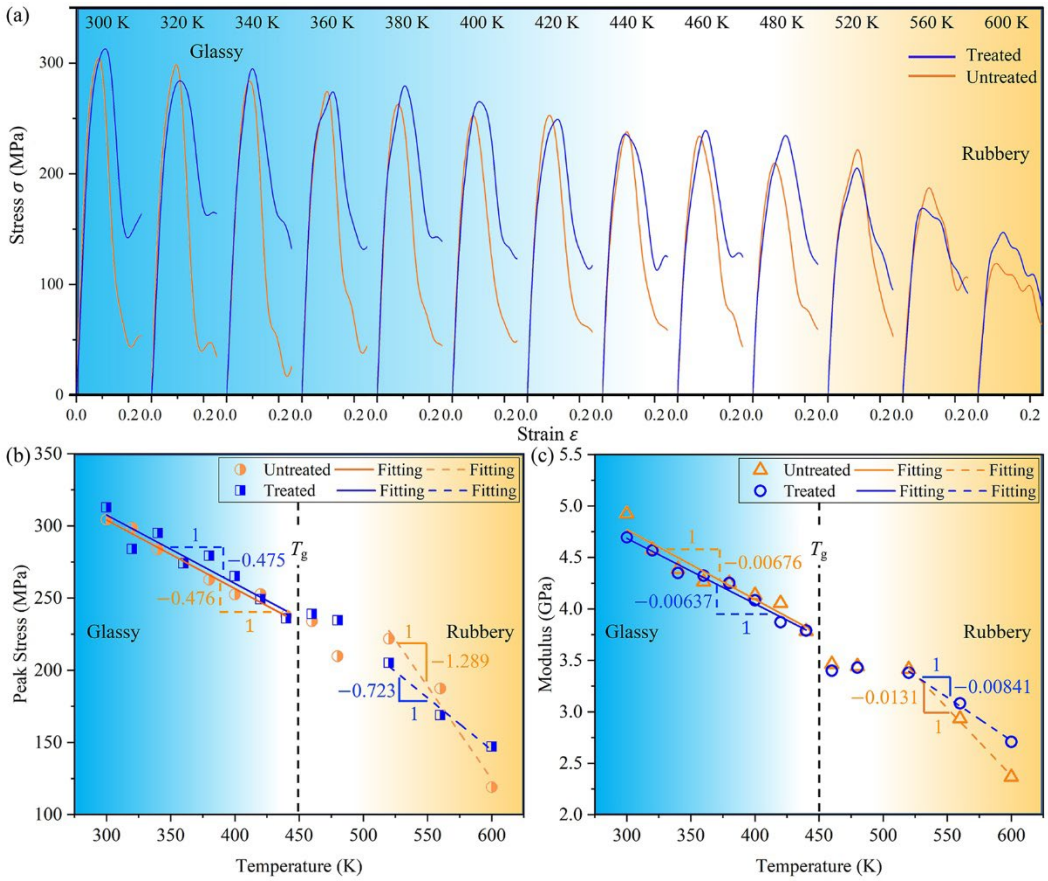

Figure 7. Comparison of the mechanical properties of the two fibre-matrix interfaces. (a) Stress-strain curves of the two fibre-matrix interfaces in the initial debonding processes at different temperatures; (b) variation of peak stress of the two interfaces with the temperature; (c) modulus of the matrix at the two interfaces at different temperatures.

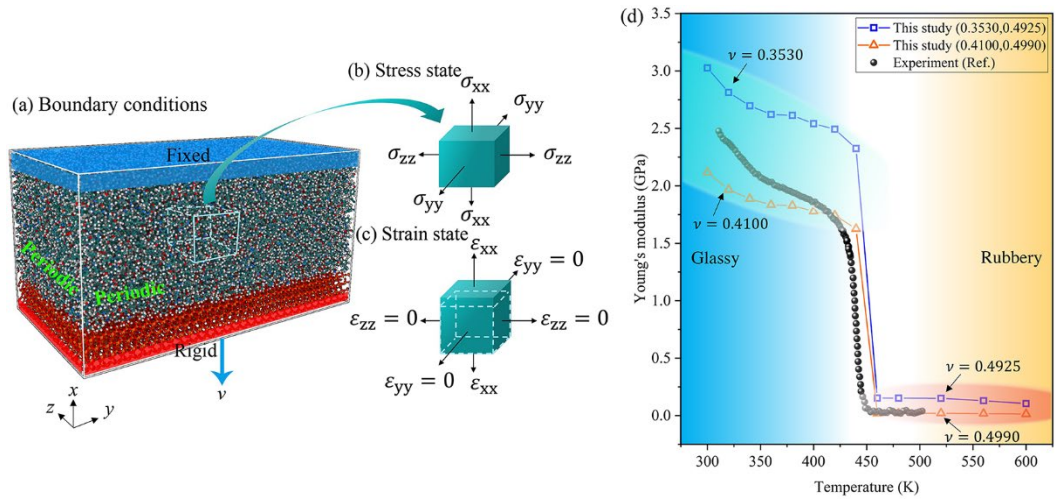

Figure 8. (a) Boundary conditions of the MD model; (b) stress state; (c) strain state; and (d) comparison of the estimated Young's modulus of the matrix in this study and experimental results from Ref. [51].

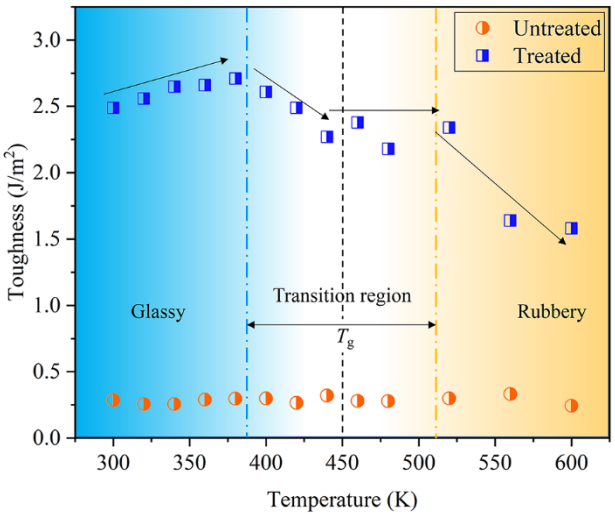

Figure 9. Variations of the interfacial toughness of the two interfaces with the temperature.

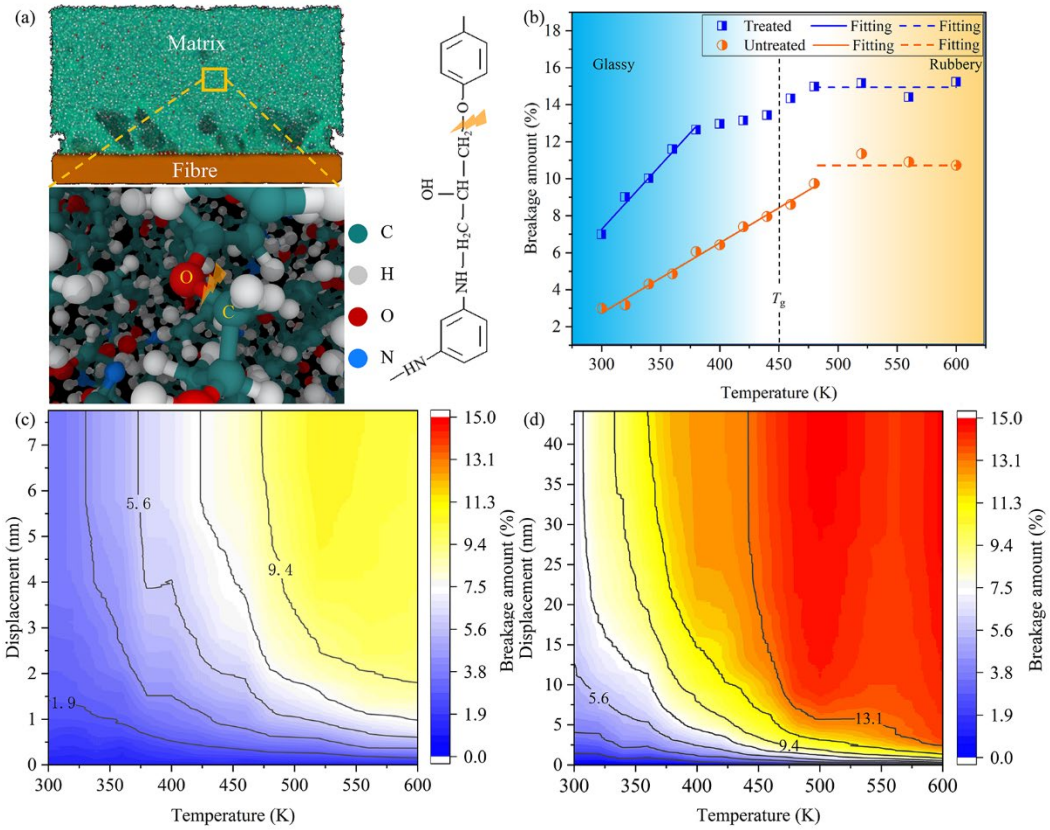

Figure 10. (a) Molecular morphology of the C-O bond (ether linkage) in the matrix; (b) total breakage amount of the C-O bonds of the two interfaces after debonding at different temperatures; and variations of the breakage amount of the C-O bonds in untreated (c) and treated (d) fibre-matrix interfaces, respectively, as a function of temperature and debonding displacement.

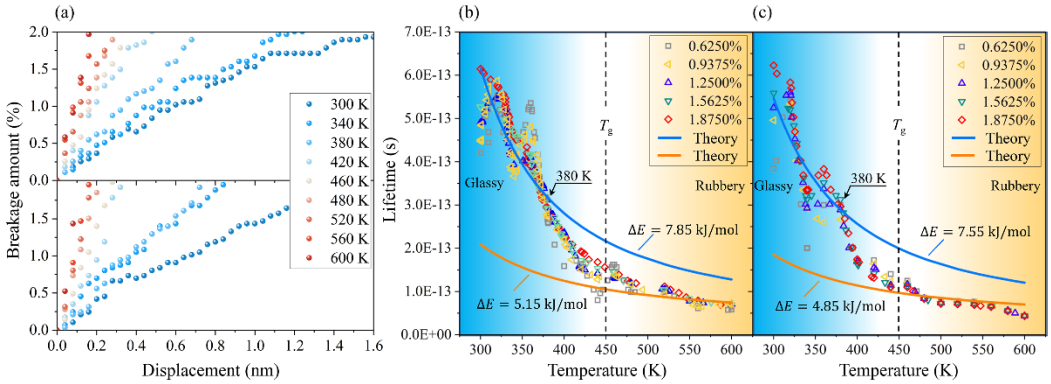

Figure 11. (a) Breakage amount of the C-O bond at the untreated interface (upper) and the sizing-treated interface (lower); the average lifetime of the C-O bonds at the untreated interface (b) and the sizing-treated interface (c) at different breakage amounts as a function of temperature: MD simulation results (scatter plots) and theoretical estimates (curves).